Optimization of power and energy densities in supercapacitors

David B. Robinson*

Sandia National Laboratories, PO Box 969 MS 9291, Livermore, CA 94551, USA

ARTICLE INFO

ABSTRACT

Supercapacitors use nanoporous electrodes to store large amounts of charge on their high surface areas, and use the ions in electrolytes to carry charge into the pores. Their high power density makes them a potentially useful complement to batteries. However, ion transport through long, narrow channels still limits power and efficiency in these devices. Proper design can mitigate this. Current collector geometry must also be considered once this is done. Here, De Levie's model for porous electrodes is applied to quantitatively predict device performance and to propose optimal device designs for given specifications. Effects unique to nanoscale pores are considered, including that pores may not have enough salt to fully charge. Supercapacitors are of value for electric vehicles, portable electronics, and power conditioning in electrical grids with distributed renewable sources, and that value will increase as new device fabrication methods are developed and proper design accommodates those improvements. Example design outlines for vehicle applications are proposed and compared.

1. Introduction

Electrochemical double-layer supercapacitors have been proposed as complements to batteries in both fixed large-scale energy storage applications as well as in electric vehicles and portable electronics [1–4]. As with any capacitor, they store energy in an electric field between a pair of conducting materials, or through a fast interfacial redox reaction. They store less energy in a given volume than batteries, but the charging and discharging rates of the latter can be limited by rates of chemical reactions and of ion transport within the electrodes. Supercapacitors do not rely on these processes, so they can deliver power more rapidly [5]. However, because they store energy only at interfaces, their electrodes must be highly porous to include a high surface area in a given volume. Ion transport through long, narrow pores, and between electrodes, can still limit charge and discharge rates. De Levie first addressed the charging rates of pores several decades ago [6,7], and many elaborations have been developed since then, with application to diverse electrode processes. The emphasis has been directed more toward electrochemical reaction kinetics and not to supercapacitor optimization [8–12]. Refinements on the version that considers only electrostatic charging include treatment of finite pore length [13,14], variable pore cross section [15], an ensemble of pores of different sizes [16], spatially nonuniform resistivity [17] and capacitance [18], and generalized impedance elements [19,20]. A model

starting from the Nernst–Planck equation has also been developed [21]. The resistivity of the electrode is often considered negligible, although this has been incorporated into the generalized models.

Newman et al. have developed porous electrode models of value for common device arrangements, including packed beds of porous particles, where typically the porous material is treated as a macroscopic medium with unique properties [22–25]. This approach has proven valuable for practical purposes, although it involves assumptions and complexities adapted for such systems. De Levie's single-pore treatment is still conceptually useful as a modular, bottom-up approach that provides a simple path to understanding of supercapacitors with near-ideal device geometries.

Since the De Levie model was first proposed, many improvements have been made toward the synthesis of electrodes with well defined nanoscale porosity and high aspect ratio [26–30] as well as electrolytes and insulating spacers with improved properties [31]. Hierarchical and interpenetrating material structures are an active area of study [32–34]. Nanoscale effects that change classical predictions of resistivity and capacitance have been predicted [35] and observed [34]. Further extension and application of the model could guide design of larger scale, faster capacitors that make use of new fabrication methods and take advantage of nanoscale effects.

Some important physical considerations for De Levie's capacitor model have been only briefly examined, including the effects of resistance outside a pore, and of the case where the electrode consumes enough ions to increase resistivity, which can be important for electrodes with nanometer-scale pores [1,7]. The implications of the model for supercapacitor design have also not been thoroughly examined from this perspective. Energy and power analyses have been performed on supercapacitors using a simple *RC* circuit model

* Tel.: +1 925 294 6613; fax: +1 925 294 3020.
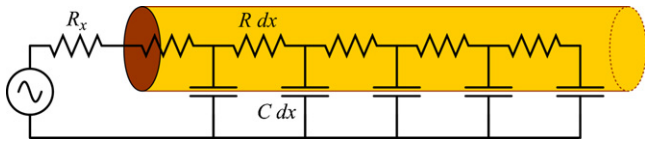 *E-mail address:* drobins@sandia.gov.

Fig. 1. Geometry of pore model. R represents resistance per unit length, while C represents capacitance per unit length; these elements are distributed continuously over a finite length.

[36,37], which is often adequate, but less so in an optimized device. Several recent reports have described the optimal design of a supercapacitor as one with hierarchically porous electrodes [38–40]. Others have pointed out that, for batteries, interpenetration of the two opposing electrodes leads to optimal power and energy densities [41]. An analysis of the relationship between geometry, pore resistance, and interelectrode resistance can help to clarify design approaches.

The capacitive case of De Levie's model for finite pores with external resistance has been understood by prior authors, but important concepts relevant to device design have not been stated, so the basics of the model are presented in Section 2. The power and energy densities are then derived for arrays of electrode pairs, which constitute a basic model of a supercapacitor. These figures of merit are analyzed as a function of model parameters for materials, device geometry, voltage, and frequency, accounting for the possibility of depletion of free ions and of power limitation by current collectors. A design strategy to obtain optimal performance is presented, providing targets for future development of fabrication methods. Example designs for electric vehicle regenerative braking are proposed.

2. De Levie model for single-pore half-cell

2.1. Background

De Levie covered the case of a semi-infinite capacitive pore [6] and briefly discussed a finite pore [7]. Keiser et al. studied the impedance of a finite pore in detail [15]. These works have been reviewed by Conway [1]. For power and energy analyses, the behavior of admittance must be carefully considered, with attention to the effect of finite pore length and external solution resistance. This is helped by an understanding of the spatial variation of current and voltage in the entire circuit. These additional aspects are described here, presented in a form easily applied to spreadsheet analysis of experimental data.

2.2. Circuit model

In a supercapacitor, pores in an electrode are closely packed, and opposing electrodes are also close. This can be treated as an array of pairs of cylindrical pores, each of length L and separated by a finite length D. Because the pair is symmetric, it can be further simplified to a one-dimensional single-pore half-cell, reflecting half of the pair. Taking $x = 0$ at the end of one pore, in the half-cell, there is a fictitious contact between the electrodes at $x = L + D/2$. The voltage V_{in} across a half-cell is half of that across a symmetric electrode pair.

De Levie treats the pore as a long prismatic electrode that behaves like a finite transmission line (Fig. 1) with resistance in the ion-conducting phase per unit length R and capacitance per unit length C. The resistivity of the electrode itself is considered negligible. Outside the pore is the external resistance R_x, representing ion

conduction between the pore entrance and a point halfway to the opposing electrode. Note that R_x is a resistance and not a resistance per unit length.

2.3. Governing equations and boundary conditions

De Levie's basic equations describing current and voltage within the pore are:

$$\frac{dV}{dx} = -IR, \qquad \frac{dI}{dx} = -C\frac{dV}{dt} \tag{1}$$

which can be combined to

$$\frac{dV}{dt} = \frac{1}{RC}\frac{d^2V}{dx^2} \tag{2}$$

by taking the spatial derivative of the resistance equation and substituting the capacitance equation. The current also obeys Eq. (2), and it is equivalent in form to the diffusion equation. Outside the pore, the current is constant, and voltage increases linearly by IR_x from the pore entrance to the cell midpoint.

Of primary interest is the current response to a sinusoidal voltage input at the pore entrance. For this, the boundary conditions at the bottom of the pore ($x = 0$) are $I(0, t) = 0$ and $V(0, t) = V_0 \cos(\omega t)$ where V_0 is arbitrary, although it is preferable to specify the voltage at the end of the pore V_L or across the entire half-cell V_{in}.

2.4. Voltage and current solutions

Solutions can be found by separating into time- and space-dependent factors $V(x)\exp(\pm i\omega t)$; substitution reveals that $V(x) = \exp(x\sqrt{\pm i\omega RC})$. Expansion of $\sqrt{i}$ allows rearrangement into purely real functions that can be written in the form $V(x, t) = \exp(\pm x\sqrt{\omega RC/2})\cos(\omega t \pm x\sqrt{\omega RC/2})$, which can be combined to satisfy the boundary conditions. These can be further rearranged into a form $|V(x)|\cos(\omega t + \angle V(x))$, which is the real part of the complex voltage $|V(x)|\exp i\angle V(x)\exp i\omega t$, and can be expressed as

$$V(x, t) = \text{Re}\, V(x)\cos(\omega t) - \text{Im}\, V(x)\sin(\omega t) \tag{3}$$

where $\text{Re}\, V = |V|\cos\angle V$ and $\text{Im}\, V = |V|\sin\angle V$. With voltage magnitude V_L normalized at the pore entrance, but phase measured versus $x = 0$, and with time constant $\tau = RCL^2$, the components are

$$\text{Re}\, V(x) = \frac{V_L \cosh((x/L)\sqrt{\omega\tau/2})\cos((x/L)\sqrt{\omega\tau/2})}{\sqrt{\cosh^2(\sqrt{\omega\tau/2}) - \sin^2(\sqrt{\omega\tau/2})}} \tag{4}$$

$$\text{Im}\, V(x) = \frac{V_L \sinh((x/L)\sqrt{\omega\tau/2})\sin((x/L)\sqrt{\omega\tau/2})}{\sqrt{\cosh^2(\sqrt{\omega\tau/2}) - \sin^2(\sqrt{\omega\tau/2})}} \tag{5}$$

The voltage at the pore entrance can be expressed in terms of bounded functions

$$V(t) = \frac{V_L \cos(\sqrt{\omega\tau/2})\cos(\omega t) - V_L \tanh(\sqrt{\omega\tau/2})\sin(\sqrt{\omega\tau/2})\sin(\omega t)}{\sqrt{1 - \sin^2(\sqrt{\omega\tau/2})\text{sech}^2(\sqrt{\omega\tau/2})}} \tag{6}$$

which can make calculations easier. The hyperbolic secant function can be taken as zero when its argument is much larger than 10.

The current can be determined by taking the spatial derivative of V and dividing by R. It is positive when the voltage is decreasing from the pore entrance to the bottom, and represents positive charge flowing from the pore entrance to the bottom.

$$\text{Re}\, I(x) = \frac{V_L\sqrt{\omega\tau/2}}{RL}\frac{[\sinh((x/L)\sqrt{\omega\tau/2})\cos((x/L)\sqrt{\omega\tau/2}) - \cosh((x/L)\sqrt{\omega\tau/2})\sin((x/L)\sqrt{\omega\tau/2})]}{\sqrt{\cosh^2(\sqrt{\omega\tau/2}) - \sin^2(\sqrt{\omega\tau/2})}} \tag{7}$$
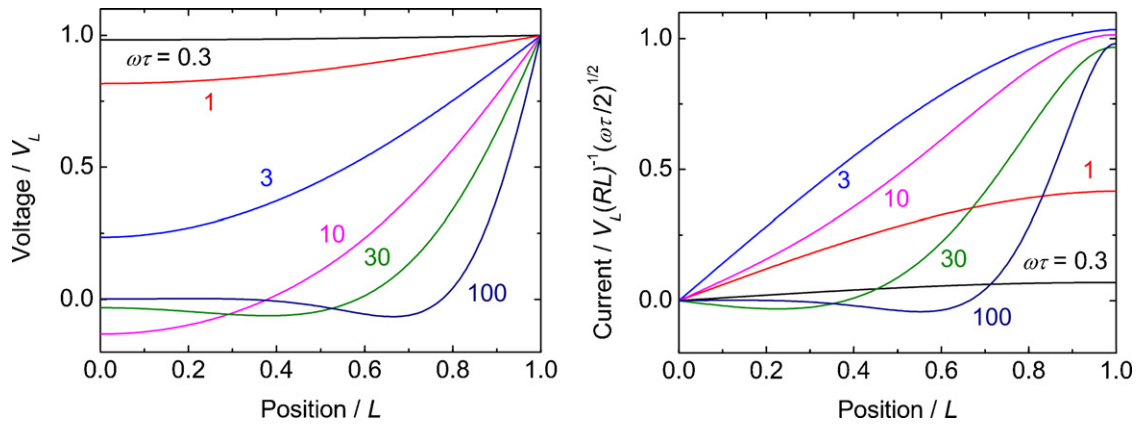
Fig. 2. Left: Voltage versus position for various frequencies at the instant where $V_L = 1$. Right: Current at the same instant versus position, normalized by the prefactor to help show the different curve shapes. Actual peak currents increase monotonically.

$$\operatorname{Im} I(x) = \frac{V_L \sqrt{\omega\tau/2}}{RL} \frac{[\sinh((x/L)\sqrt{\omega\tau/2})\cos((x/L)\sqrt{\omega\tau/2}) + \cosh((x/L)\sqrt{\omega\tau/2})\sin((x/L)\sqrt{\omega\tau/2})]}{\sqrt{\cosh^2(\sqrt{\omega\tau/2}) - \sin^2(\sqrt{\omega\tau/2})}} \tag{8}$$

Again, a simpler form is obtained for the value at the pore entrance.

$$\operatorname{Re} I = \frac{V_L \sqrt{\omega\tau/2}}{RL} \frac{[\tanh(\sqrt{\omega\tau/2})\cos(\sqrt{\omega\tau/2}) - \sin(\sqrt{\omega\tau/2})]}{\sqrt{1 - \sin^2(\sqrt{\omega\tau/2})\operatorname{sech}^2(\sqrt{\omega\tau/2})}} \tag{9}$$

$$\operatorname{Im} I = \frac{V_L \sqrt{\omega\tau/2}}{RL} \frac{[\tanh(\sqrt{\omega\tau/2})\cos(\sqrt{\omega\tau/2}) + \sin(\sqrt{\omega\tau/2})]}{\sqrt{1 - \sin^2(\sqrt{\omega\tau/2})\operatorname{sech}^2(\sqrt{\omega\tau/2})}} \tag{10}$$

In the space between electrodes, the current is constant, and the voltage extends linearly by

$$V(x, t) = V(L, t) + I(L, t)R_x \frac{(x - L)}{(D/2)} \quad L < x < \frac{D}{2} \tag{11}$$

Much of the range of behavior of voltage and current within the pore is shown in Fig. 2. At low frequencies, the voltage is independent of position, and the current decreases linearly in the pore, traveling an average distance of $L/3$ into the electrode. At high frequencies, damped voltage and current waves propagate into the pore, and both are approximately zero at the bottom of the pore. A transition between the two occurs between $\omega = 1/\tau$ and $10/\tau$.

2.5. Admittance and impedance

The admittance is the complex ratio of current to voltage and is a helpful way to understand pore behavior; when incorporating R_x, it is experimentally accessible, and is important for understanding power and energy densities. For the pore alone, it can be expressed as

$$\operatorname{Re} Y = \frac{\sqrt{\omega\tau/2}}{RL} \frac{\tanh\sqrt{\omega\tau/2} - \cos\sqrt{\omega\tau/2}\sin\sqrt{\omega\tau/2}\operatorname{sech}^2\sqrt{\omega\tau/2}}{1 - \sin^2\sqrt{\omega\tau/2}\operatorname{sech}^2\sqrt{\omega\tau/2}} \tag{12}$$

$$\operatorname{Im} Y = \frac{\sqrt{\omega\tau/2}}{RL} \frac{\tanh\sqrt{\omega\tau/2} + \cos\sqrt{\omega\tau/2}\sin\sqrt{\omega\tau/2}\operatorname{sech}^2\sqrt{\omega\tau/2}}{1 - \sin^2\sqrt{\omega\tau/2}\operatorname{sech}^2\sqrt{\omega\tau/2}} \tag{13}$$

The external resistance can be added to $1/Y$; the circuit admittance is $Y_x = Y/(1 + R_xY)$ or

$$\operatorname{Re} Y_x = \operatorname{Re} Y + \frac{R_x|Y|^2}{(1 + R_x \operatorname{Re} Y)^2 + (R_x \operatorname{Im} Y)^2} \tag{14}$$
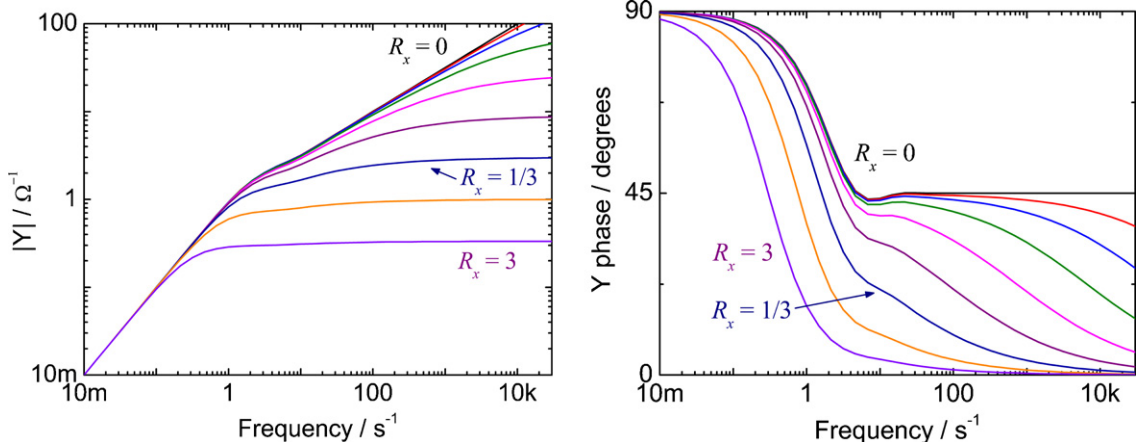

Fig. 3. Admittance magnitude (left) and phase (right) for unit pore half-cell ($RL = 1\,\Omega$, $CL = 1\,\text{F}$) and external solution resistance R_x in Ω varying by factors of 3.
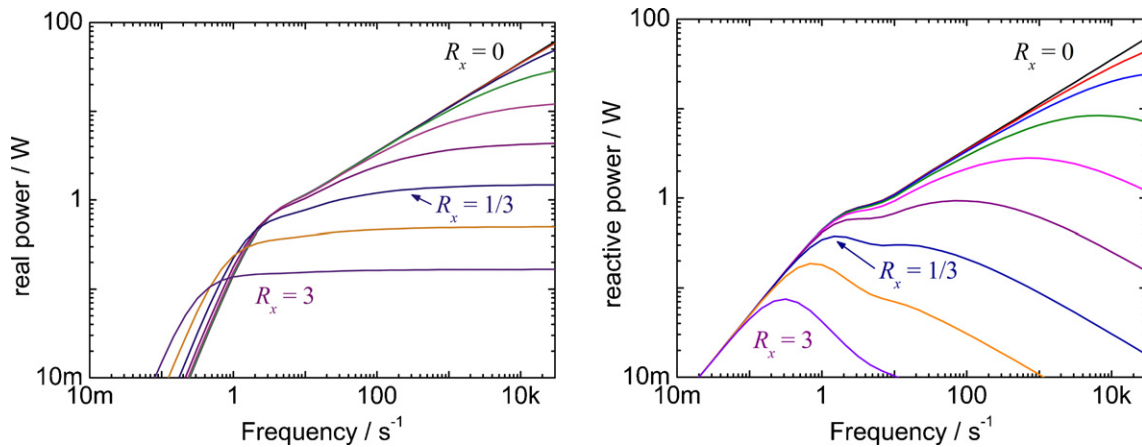
Fig. 4. Real power (left) and reactive power (right) for unit pore half-cell ($RL = 1\,\Omega$, $CL = 1\,$F) where $V_{in} = 1\,$V and external solution resistance R_x in Ω varies by factors of 3.

$$\operatorname{Im} Y_x = \frac{\operatorname{Im} Y}{(1 + R_x \operatorname{Re} Y)^2 + (R_x \operatorname{Im} Y)^2} \qquad (15)$$

(The symbol Y, not Y_x, is used for the circuit admittance henceforth.) While admittance is most useful for energy and power analyses, incorporating R_x is easier using the impedance, which is the complex ratio of voltage to current. In fact, De Levie noted that this can take the very compact form $Z = R_x + (RL/\sqrt{i\omega\tau})\coth\sqrt{i\omega\tau}$ [7]; the expanded form appears elsewhere [1,15]. Given the circuit impedance, circuit admittance can be obtained from $\operatorname{Re} Y = \operatorname{Re} Z/|Z|^2$ and $\operatorname{Im} Y = -\operatorname{Im} Z/|Z|^2$.

The shapes of the admittance magnitude and phase are shown in Fig. 3. At low frequencies, when the pore charges completely, the admittance magnitude is ωCL and phase is 90°. At intermediate frequencies, if R_x is negligible, the admittance magnitude is $\sqrt{\omega C/R}$ and phase is 45°; charging does not depend on length because the pore is charging incompletely. The transition to this occurs between $\omega = 1/\tau$ and $10/\tau$, as observed in Fig. 1. However, if external resistance is high, most of the voltage drop occurs there and the electrode behaves like a discrete RC circuit, with a high-frequency admittance of $1/R_x$ and no high-frequency phase shift. While the distributed RC effect from the pores is easily observed in conventional Nyquist impedance plots, its effect in Bode plots of the admittance is mostly obscured when R_x is larger than $RL/3$, the maximum value of $\operatorname{Re} Z$ for the pore [15].

3. Power, energy, and efficiency of pore half-cell

A capacitor made from porous electrodes is a linear system. From the frequency response of admittance and impedance, one can easily gain knowledge of response to any signal that is a superposition of frequencies. Power and energy are not linear, so this generality is lost, but the frequency response still provides information about charge and discharge timescales. Other waveforms have been considered using simpler [42] or more complex [22] circuit models. The power S is the product of the time-dependent voltage and current:

$$S = V_{in}\cos(\omega t) \cdot V_{in}[\operatorname{Re} Y \cos(\omega t) - \operatorname{Im} Y \sin(\omega t)] \qquad (16)$$

$$S = \frac{V_{in}^2}{2}[\operatorname{Re} Y(1 + \cos(2\omega t)) - \operatorname{Im} Y \sin(2\omega t)] \qquad (17)$$

The first term in the brackets accounts for the real power, which flows only in one direction, is dissipated as heat by the resistance, and has a finite average value of $(1/2)V_{in}^2 \operatorname{Re} Y$. The second term accounts for the reactive power, which is alternately accepted and delivered by the capacitance, charging and discharging with each polarity in a cycle. Because it flows equally in both directions, its

average over a cycle is zero, but for charging only it is $(1/\pi)V_{in}^2 \operatorname{Im} Y$. The complex power $YV_{in}^2/2$ captures the real and reactive power without including the average value.

The complex power components are shown in Fig. 4. At finite R_x, peaks are observed in the reactive power, suggesting optimal operating points. One peak appears at the point where the phase crosses through 45°, and the two components are equal, representing an impedance-matched condition. When that resistance is small compared to RL, the power is near its optimum over a broad range of frequencies. A higher peak power appears at higher frequencies when R_x is less than 0.23 (a value determined numerically). However, under these conditions, real power is also high and increasing with frequency. To operate at steady state in this regime, it may be necessary to dedicate device volume to heat dissipation, which would reduce power density, although this high-frequency behavior may be useful for accommodating occasional transients.

The energy stored in the capacitor is the integral of the reactive power starting from $t = 0$:

$$E = \frac{1}{2}CLV_{in}^2\left(\frac{RL}{\omega\tau}\operatorname{Im} Y\right)\cos^2(\omega t) \qquad (18)$$

The peak instantaneous value of the stored energy is shown in Fig. 5 with a linear ordinate, highlighting the significance of the rolloff near $1/\tau$. At high R_x, the rolloff occurs instead at $1/R_x CL$ and is steeper at high frequencies than when R_x is small. Fig. 6 also illustrates the tradeoff between power and energy as frequency is increased from the bottom right to left. The power peaks when stored energy is about half its low-frequency value, except below $R_x/RL = 0.23$, when a higher peak occurs as discussed above.

Efficiency η can be defined as the ratio of energy recovered from the capacitor after a charge–discharge cycle (the peak energy shown in Fig. 5) to energy given to the capacitor, which is that plus the integral of real power over that time.

$$\eta = \frac{\operatorname{Im} Y}{\pi \operatorname{Re} Y + \operatorname{Im} Y} \qquad (19)$$

The frequency dependence of cycle efficiency is shown in Fig. 6. It resembles the shape of the admittance phase, but rolls off less steeply. For the efficiency of charging only (not the whole cycle), the $\operatorname{Re} Y$ term is divided by 2; this doubles the high-frequency values and increases intermediate values.

4. Device geometry; energy and power density

4.1. Device geometry

A macroscopic supercapacitor can be modeled by considering a parallel array of pore pairs: a device composed of two planar elec-
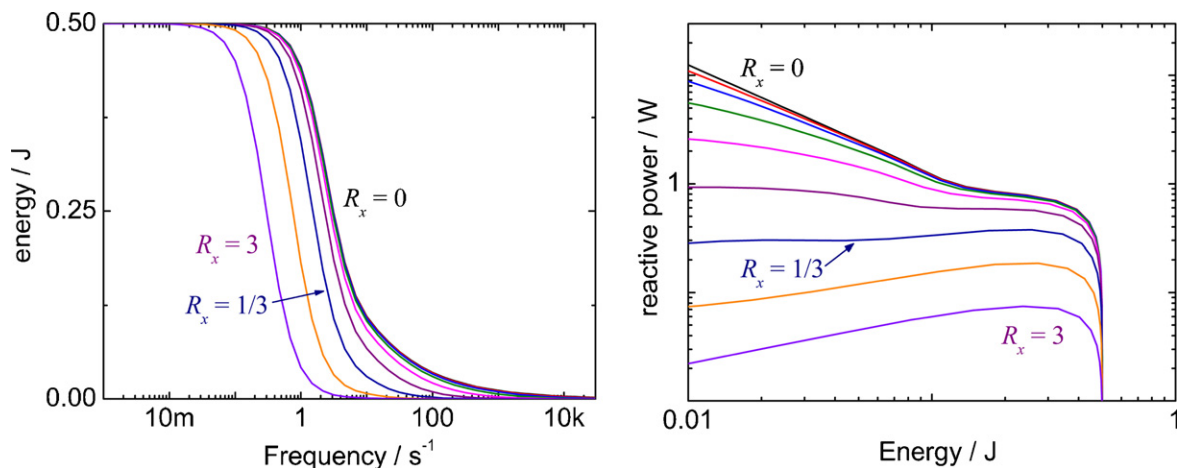
Fig. 5. Left: Energy stored in unit pore half-cell ($RL = 1\,\Omega$, $CL = 1$ F) and external solution resistance R_x in Ω varying by factors of 3. Right: Reactive power versus energy, combining the curves in the left plot with those in Fig. 4.

trodes, each with a thickness L, separated by a distance D by an ion-conducting phase and connected across a load or source. Each electrode contains an array of closely packed cylindrical pores of radius r. A porosity parameter P represents the fraction of the electrode surface area occupied by pore entrances, which for cylindrical pores is the same as the volume fraction. Table 1 gives values of this parameter for various pore arrangements.

The hexagonal geometry spaced by 1–2 radii is frequently observed in porous alumina, block copolymers, and surfactant-templated materials [43]. Dealloyed nanoporous gold is a useful test material among porous conductors. Although its pores are disordered and not cylindrical, high aspect ratios r/L can be achieved [44]. Electron tomography has shown that the typical pore volume fraction is 0.5 [26].

This planar electrode pair can presumably be stacked, rolled or pleated (or a combination of these) to fill a given volume [45]. Stacking electrodes puts capacitors in series, increasing operating voltage without increasing current. Rolling or pleating puts capacitors in parallel, increasing current but not voltage. Two half-cell electrodes with closed-ended pores placed back-to-back are equivalent to a single electrode of the same thickness with open-ended pores, assuming that each opening faces an equivalent counterelectrode pore [7]. This arrangement can be obtained in rolling, and in pleating except at corners. It could be achieved in stacking, except that the midpoint of the pore must be blocked to prevent ion transport, because in this case each electrode is an anode on one side

and cathode on the other. These arrangements of electrode pairs provide building blocks for a three-dimensional device.

4.2. Dependence of circuit parameters on geometry

To predict performance of a device design, the resistance and capacitance per unit length of a pore can be expressed as $R = \rho/\pi r^2$ and $C = 2\pi r C_{dl}$, resulting in time constant $\tau = 2\rho C_{dl} L^2/r$, where r is the pore radius, ρ is the solution resistivity, and C_{dl} is the capacitance per unit area of a planar interface made from the same materials [15]. If parallel cylindrical pores are packed closely with a porosity parameter P, the number of pores per unit volume is $P/\pi r^2 L$ and multiplying this by CL gives capacitance per unit volume $C_{vol} = 2PC_{dl}/r$. Multiplying by L gives capacitance per unit electrode area $C_{area} = 2PC_{dl}L/r$. Similarly, dividing RL by $P/\pi r^2$ gives an area resistance $R_{area} = \rho L/P$. The product of R_{area} and C_{area} gives the characteristic time of a single pore.

For an isolated pore, the external resistance would be similar to that of a microelectrode $R_x = \rho/2\pi r$ [46]. However, pores in a supercapacitor are packed closely, and the current path available to each pair of pores is narrow. Typically $D \gg r$, and the interelectrode region generally contains an insulating spacer with porosity P_x, so the current path available to each single-pore half-cell is contained by a prism of length $D/2$ and wider than the pore area by a factor P_x/P. The external area resistance is then $R_{x,area} = \rho D/2P_x$. To obtain the macroscopic current density, area impedance, admittance per unit area, or related functions, one simply substitutes R_{area} for RL, C_{area} for CL, and $R_{x,area}$ for R_x in the relevant equation. Experimental data can be fit to these to obtain estimates of parameters and compared to design predictions.

4.3. Power and energy densities

The main figures of merit for energy storage devices are energy density and power density. These can be obtained from the energy and power per unit volume by dividing by the thickness of the half-cell $L + D/2$. They can be written as products of dimensionless functions of dimensionless parameters $\omega\tau$, $(D/2L) = (R_{x,area}/R_{area})(P_x/P)$, and prefactors that affect the ordinate scale in Fig. 7:

$$E = \frac{C_{vol}V_{in}^2}{2}\frac{R_{area}\,\mathrm{Im}\,Y}{\omega\tau(1 + D/2L)}, \qquad S = \frac{C_{vol}V_{in}^2}{\tau}\frac{R_{area}\,\mathrm{Im}\,Y}{(1 + D/2L)} \qquad (20)$$

As Fig. 7 shows, energy and power density decrease and drop off more sharply as R_x increases.
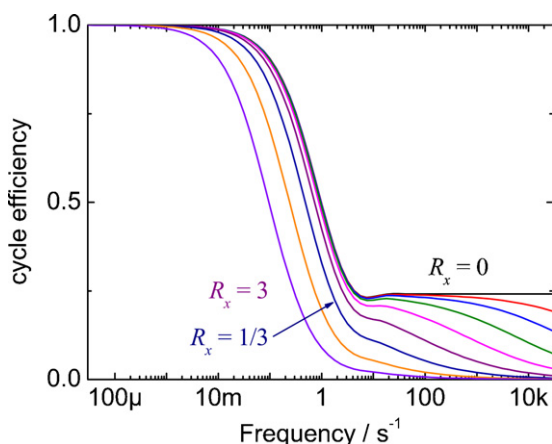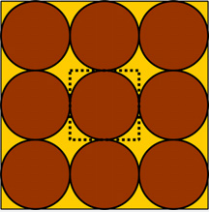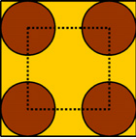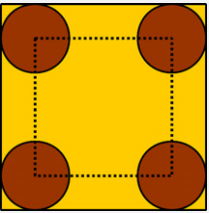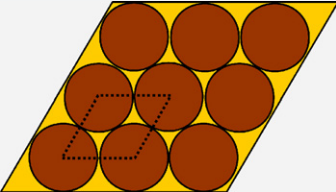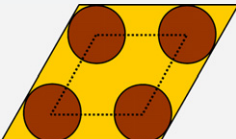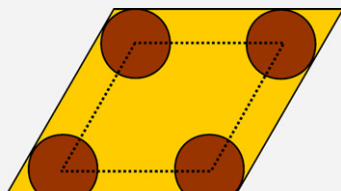

Fig. 6. Cycle efficiency of unit pore half-cell ($RL = 1\,\Omega$, $CL = 1$ F) where external solution resistance R_x in Ω varies by factors of 3.

Table 1
Porosity parameter P for various arrangements of cylindrical pores. The spacing is in units of pore radius. Dotted line indicates unit cell.

	Spacing	P
	0	$\pi/4 = 0.79$
	1	$\pi/9 = 0.35$
	2	$\pi/16 = 0.20$
	0	$\pi/2\sqrt{3} = 0.91$
	1	$2\pi/9\sqrt{3} = 0.40$
	2	$\pi/8\sqrt{3} = 0.23$

4.4. Energy density scaling limits: electrolyte capacity

Holding $\omega\tau$ constant, decreasing r increases E without changing S. Apparently, once r and D are made as small as possible, L can be chosen to tune the frequency of peak power, resulting in an optimal device. However, lower bounds exist for r and D because the electrolyte must contain enough ions to charge the capacitive interface. The number of monovalent ions in a complete single-pore cell (both electrodes) is $2\pi r^2 L[1 + (D/2L)(P_x/P)]c$ where c is the salt concentration, and the number needed to fully charge a pore is $2\pi r L C_{dl} V_{in}/F$, where F is Faraday's constant, so there is just enough salt to charge the pore when

$$\frac{D}{2L} = \frac{P}{P_x}\left(\frac{r^*}{r} - 1\right) \tag{21}$$

$$r^* = \frac{C_{dl}V_{in}}{Fc} \tag{22}$$

If $r > r^*$, there are already enough anions and cations in the two pores to charge each of them. However, the resistivity also depends on concentration, and concentration of unbound ions will drop significantly under this condition [1,7]. An appropriate margin should be included in device design. The salt concentration will generally be near saturation, typically 1 M, and the voltage is bound by the redox breakdown voltage of the electrolyte, typically 1–4 V. For 1 M, 1 V and $C_{dl} = 20\,\mu\text{F cm}^{-2}$ (a typical value for a metal–electrolyte interface [47]), a 4 nm diameter pore contains just enough salt. At or below that point, D must be increased to provide a salt reservoir, resulting in

$$E = \frac{PC_{dl}V_{in}^2}{(1 - P/P_x)r + (P/P_x)r^*}\frac{R_{area}\,Im\,Y}{\omega\tau} \tag{23}$$

The second term in the denominator limits the energy density benefit of decreasing pore diameter; the prefactor can be no larger than FcV_{in}, the extreme case where the interelectrode spacing dominates the volume and all ions of each sign participating in charging. When $r = r^*$, it is already that times P, the case where interelectrode spacing is negligible. Because D and R_x increase as r decreases, the rolloff of the dimensionless part sharpens and moves to lower frequency, and maximum power is decreased. Fig. 8 shows the effect of increasing V_{in} so that the critical radius is exceeded. Instead of increasing quadratically, the energy density creeps upward only slightly at low-frequency, and the high-frequency behavior is attenuated as noted. Power density behaves similarly, although the resistivity increase, not accounted for here, would cause further limitation.

This suggests an alternative design approach, assuming that one wants to maximize energy density without paying a significant
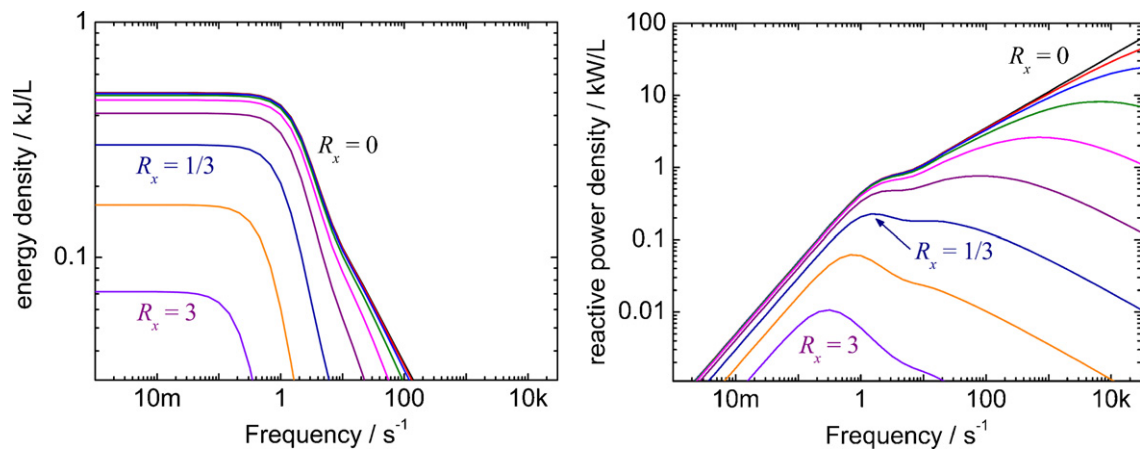

Fig. 7. Energy density (left) and power density (right) of unit-porous electrode half-cell ($R_{area} = 1\,\Omega\,\text{cm}^2$, $C_{area} = 1\,\text{F cm}^{-2}$) where $V_{in} = 1$ V and external solution resistance $R_{x,area}$ in $\Omega\,\text{cm}^2$ varies by factors of 3. Porosity ratio P/P_x is 0.5 and L is 1 cm.
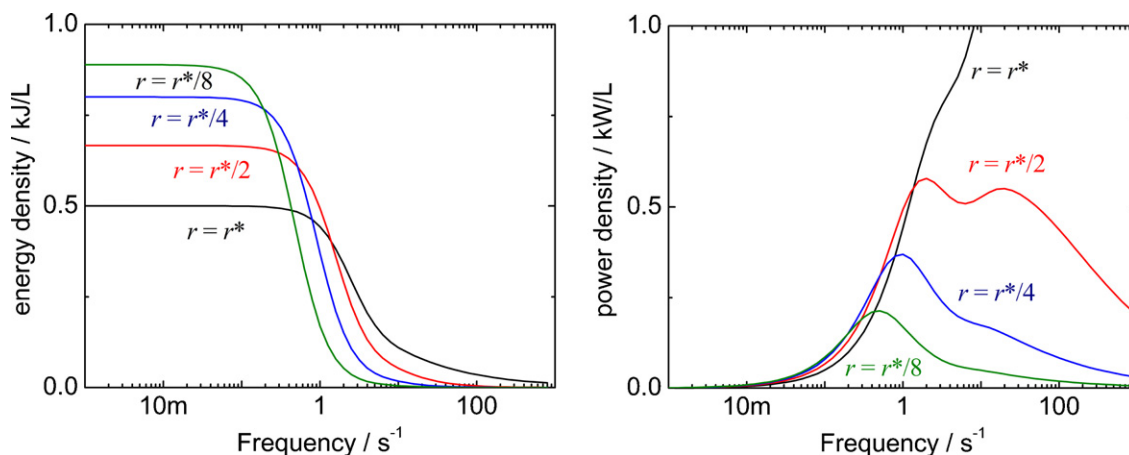
Fig. 8. Energy density (left) and power density (right) as voltage is increased, thereby increasing the critical radius r^*. Other parameters remain the same as Fig. 7.

power density penalty. The pore radius should be at or above the critical radius, and the electrode spacing should be kept as small as practical. Again, L can be chosen to tune the frequency of peak power. To incorporate a margin m to prevent salt depletion from slowing charging time, an alternative radius is computed (m is perhaps 2 or 3):

$$r = \frac{mr^*}{(1 + (D/2L)(P_x/P))} \tag{24}$$

With other parameters fixed, the pore radius should be the greater of this value and r^*. In some cases, specifically adsorbed ion pairs on the pore walls may serve as a reservoir that keeps resistivity low without the need for this margin [48,49]. However, the effect of this on conductivity in pores is in need of further study. Furthermore, other nanoscale effects including resistivity increases due to pore wall interactions [35], or capacitance changes due to double-layer overlap [50] or ion desolvation [51] are glossed over by applying this margin; each of these effects provides opportunities for further optimization.

4.5. Power density scaling limits: current collection

As the previous section notes, the power density prefactor is not usefully adjusted by r. However, it is strongly affected by L. The assumption has been made that charge is stored only pore walls, and current paths cannot be meaningfully less than the pore radius. So, $L = r^*$ is an extreme case where D can still be less than or equal to L. At $\omega = 1/\tau$, the power is near the peak value, and the energy density is near half its low-frequency value, depending on the value of D.

$$S \approx \frac{C_{vol}V_{in}^2}{2\tau} = \frac{P(Fc)^2}{2\rho C_{dl}^2} \tag{25}$$

For the example in the previous section, and taking $\rho = 1\,\Omega$ cm, this number exceeds $10^{15}\,\mathrm{W\,L^{-1}}$.

In general, IR drop through electrodes, current collectors, or device contacts will limit this. The electrode resistivity ρ_m has been assumed zero, but will generally not be below $20\,\mu\Omega$ cm, a typical value for metals. The approximation is fair along the length of a pore, but not necessarily for delivering to a remote load. In analogy to the low-frequency pore area resistance $\rho L/3P$ and the interelectrode area resistance $\rho D/2P_x$, an electrode area resistance is $\rho_m L_m$ where L_m is the distance to the load. The ratio of L_m to $(L/3P + D/2P_x)$ should be less than ρ/ρ_m to avoid limiting power. If it is desirable to make the device leads narrower than the overall device, L_m must be reduced in proportion to that area ratio and the leads tapered to maintain a pathway to each pore.

Passing current perpendicular to the pores is necessary for pleated or rolled structures, and involves a scaling limit. The lateral current through the electrode experiences a sheet resistance of approximately $\rho_m/(1-P)L$, with some dependence on pore geometry. Comparing to the area resistance of the pores shows that the aspect ratio L_{pleat}/L of this pathway must be kept below $\sqrt{(\rho/3\rho_m)(1-P)/P}$ to avoid limiting power. Also, in this case the distance to a thicker conductor must be comparable to L_{pleat}. This is about 100 with the above values, and will limit the use of rolls or pleats to increase device volume or make a device more compact.

A device composed of stacked electrodes faces a different limit. The operating voltage and device resistance increase in proportion to the number of layers. This number will be limited by fabrication cost and the voltage requirements of the external circuit, and 100 may be a representative value for that. At the top and bottom of the stack, a budget of ρ/ρ_m applies for reduction of area and extension of length of the contact conductor versus an electrode layer, as described above. To increase device volume beyond that limit, power must be increased by increasing the area of each electrode, and also the area of the contacts. Stacking and pleating can be combined to keep the device compact, as long as the area of the end layers of the stacks embedded within the pleats is accounted for in the budget.

One or two dimensions of a maximum-power device are thus bound. The energy stored by a cube-shaped maximum-power capacitor, according to the above example, is limited to $PFcV(100r^*)^3$ which is 0.4 pJ. More generally, there will often be a tradeoff between capacitor geometry and achieved power. Fig. 9 illustrates the device geometries outlined here that address this. These certainly present a challenge to fabricate economically, although as noted in the introduction, rapid progress is being made on relevant techniques, and the strategy proposed here may help guide that.

5. Example application

5.1. Materials

In an example application the following assumptions are made. It is possible to fabricate electrodes of any desired geometry, but material constraints exist: $C_{dl} = 20\,\mu\mathrm{F\,cm^{-2}}$ and $\rho_m = 20\,\mu\Omega$ cm are representative values for electrode materials of interest, $P = 0.5$, and electrode materials do not limit the voltage stability window. Important electrolyte parameters are the voltage stability window of a solute and solvent combination, the concentration of anions and cations (assumed the same here), and the resistivity. Table 2 presents representative values for an aqueous electrolyte at about
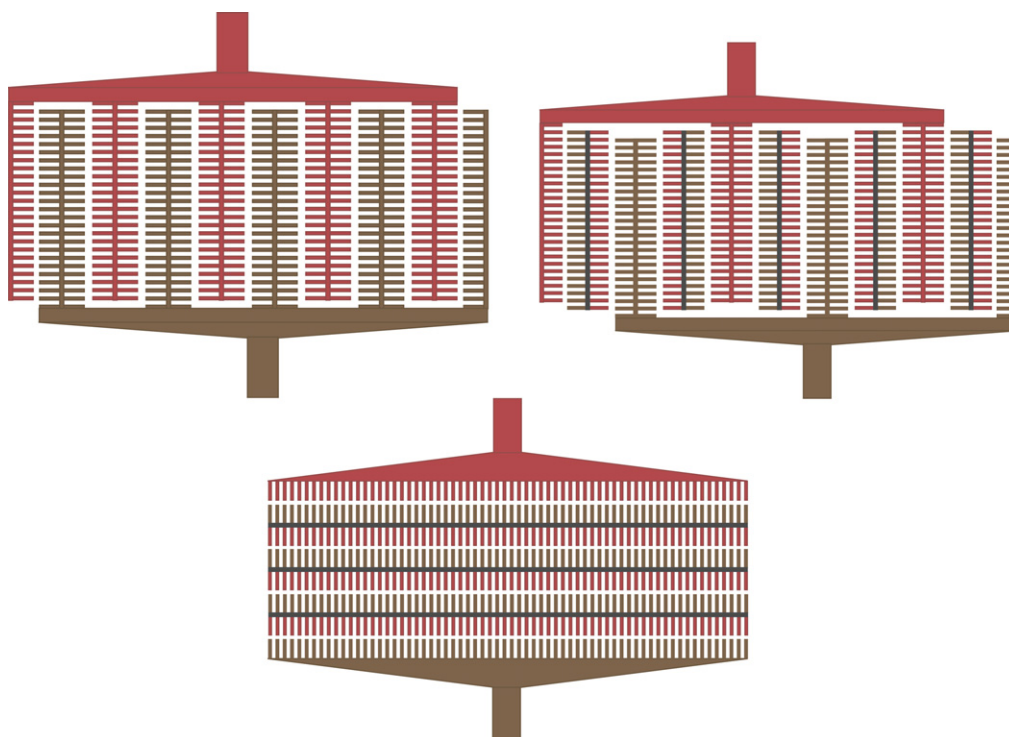
Fig. 9. Schematic of pleated (left), stacked (center), and hierarchical (right) electrode arrangements within a device.

the maximum known conductivity; a nonaqueous electrolyte, in which ion concentrations and conductivities are lower but voltage windows are higher; and an ionic liquid, which has a higher ion concentration but higher resistivity due to high viscosity [52]. Note that the stability window applies to the electrode pair, so this is double the half-cell voltage. The critical radius computed for each case is reported. Because these are liquids, a porous spacer membrane is needed. A commercial product (Celgard) is 25 μm thick with a porosity of about 0.5. For the example, a 10 μm thickness is used.

The critical radius was defined for monovalent salt. Not much advantage would be gained by using divalent salts such as magnesium sulfate, because their solubilities or concentrations of maximum conductivity (above which they are partially nondissociated) are generally lower than monovalent salts. Other ionic liquids like choline lactate have higher ion concentration (lower molar volume) but these have higher melting points and narrower stability windows.

5.2. Example: regenerative braking in electric vehicles

A 1500 kg vehicle traveling 108 km h^{-1} (30 m s^{-1}) encounters a stop sign and must recover 675 kJ kinetic energy in 10 s (67.5 kW) and reuse the energy shortly thereafter. The supercapacitor storing this energy does not experience a steady-state sinusoid as a result, but the frequency response information presented here will be used as approximations of behavior at the given timescale. A maximum operating voltage of 500 V is assumed, but to narrow the scope of the problem, other vehicle circuit characteristics are ignored, such

as the ability of the motor to deliver this power [4]. For efficiency, it is desirable to operate below the peak power frequency and near maximum energy density. However, an unnecessarily high value of τ will impose inconvenient constraints on device geometry and likely increase fabrication cost. From Fig. 6, if $\tau = 0.3$ s and R_x is low, the device is about 95% efficient on a 10 s timescale, so about 34 kJ is dissipated. In Table 3, an electrode thickness is computed to achieve this time constant from the parameters in Table 2. A salt depletion margin of 2 is used, and the pore radius and length are computed from Eq. (24) and definition of τ in Section 4.2. This makes the radius roughly $2r^*$, and allows slightly thicker electrodes to be used, which improves the external to internal resistance ratio. Because the ratio of D to L is larger for the ionic liquid, the extra ions between the electrodes allow the radius to be slightly smaller. The energy density is close to its low-frequency value under these conditions. Table 3 reports the corresponding capacitor volumes necessary to capture the vehicle's energy. The combination of high ion concentration and high voltage stability makes the ionic liquid preferable by this criterion. If the volumetric heat capacity is about 1.5 kJ (L K)$^{-1}$ (near that of organic solvents and graphite), or 2.5 for a capacitor composed of graphite and aqueous electrolyte, the device warms by the amounts shown in Table 3. These numbers account for the effect of resistance ratio on efficiency.

If the operating voltage is fixed at 500 V, the ionic liquid electrode stack is much thinner than the others because the electrodes are thinner and carry more voltage per layer. The aqueous device is relatively compact after stacking. The others could be made more compact by pleating. Table 3 reports the pleat aspect ratio (with

Table 2
Representative (not precise) parameters for three electrolyte categories. The nonaqueous solvent is a mixture of propylene carbonate and dimethoxyethane. Ionic liquid data are from BASF product literature.

	5.7 M HCl Aqueous	1 M LiClO$_4$ Nonaqueous	BMIM TFSI Ionic liquid
Stability window (V)	1.4	4.5	5
Ion concentration (M)	5.7	1	3.4
Resistivity (Ω cm)	1.2	100	300
Critical radius (nm)	0.5	9	3

Table 3
Design parameters for supercapacitors optimized to capture vehicle braking energy (675 kJ in 10 s with time constant = 0.3 s).

	5.7 M HCl Aqueous	1 M LiClO$_4$ Nonaqueous	BMIM TFSI Ionic liquid
r (nm) for $m = 2$	0.48	8.5	2.4
L (μm) for $m = 2$	95	44	14
$R_{x,area}/R_{area}$	0.053	0.11	0.37
Volume (L)	6.9	12.6	3.6
ΔT (K)	1.4	1.5	8.1
Stack height (cm)	7.1	1.1	0.37
Stack width (cm)	31	108	99
Pleat aspect ratio	0.19	5.2	8.2

respect to stack height) at which electrode resistance becomes significant. These are longer for nonaqueous electrolytes due to their higher resistivity. This would allow each to be pleated or rolled into a form about as compact as the aqueous device. At this voltage, the capacitors must be connected by short, thick conductors to operate at peak power. To be 1 m long, the leads must be more than 2 cm in diameter.

6. Conclusion

De Levie's model for porous electrodes is a valuable conceptual starting point for the design of supercapacitors, and perhaps some forms of electrolytic capacitors [53]. Its application allows for an understanding of the performance limits of these devices as measured by energy density, power density, and efficiency as a function of frequency and material and geometric parameters. Supercapacitors can be designed that maximize the use of electrolyte ions to achieve optimal energy density. Very high power densities are possible, but require thin electrode layers and device geometries. Within constraints, more compact capacitors can be formed by use of stacking, folding, and hierarchical combinations of these. Economical fabrication of these structures will require continued progress in method development. This progress will surely continue, especially as demand arises for high-power storage systems for renewable energy, vehicle, and personal electronics applications. Applied and extended versions of De Levie's model can be a valuable and quantitative guide to that work.

Acknowledgment

References

[1] B.E. Conway, Electrochemical Supercapacitors, Kluwer Academic/Plenum Publishers, New York, 1999.
[2] A. Burke, Journal of Power Sources 91 (2000) 37–50.
[3] J. Schindall, IEEE Spectrum 44 (2007) 42–46.
[4] J.M. Miller, Apec 2003: Eighteenth Annual IEEE Applied Power Electronics Conference and Exposition, vols. 1 and 2, 2003, pp. 23–29.
[5] B.E. Conway, Journal of the Electrochemical Society 138 (1991) 1539–1548.
[6] R. De Levie, Electrochimica Acta 8 (1963) 751–780.
[7] R. De Levie, in: P. Delahay, C.T. Tobias (Eds.), Advances in Electrochemistry and Electrochemical Engineering, vol. 6, Interscience, New York, 1967, pp. 329–397.
[8] R. Darby, Journal of the Electrochemical Society 113 (1966) 392–396.
[9] F. La Mantia, J. Vetter, P. Novak, Electrochimica Acta 53 (2008) 4109–4121.
[10] G. Paasch, K. Micka, P. Gersdorf, Electrochimica Acta 38 (1993) 2653–2662.
[11] F.A. Posey, T. Morozumi, Journal of the Electrochemical Society 113 (1966) 176–184.
[12] E.A. Grens, Electrochimica Acta 15 (1970) 1047–1057.
[13] F.A. Posey, Journal of the Electrochemical Society 111 (1964) 1173–1181.
[14] M. Yaniv, A. Soffer, Journal of the Electrochemical Society 123 (1976) 506–511.
[15] H. Keiser, K.D. Beccu, M.A. Gutjahr, Electrochimica Acta 21 (1976) 539–543.
[16] H.K. Song, Y.H. Jung, K.H. Lee, L.H. Dao, Electrochimica Acta 44 (1999) 3513–3519.
[17] P.H. Nguyen, G. Paasch, Journal of Electroanalytical Chemistry 460 (1999) 63–79.
[18] J. Bisquert, Physical Chemistry Chemical Physics 2 (2000) 4185–4192.
[19] J. Bisquert, G. Garcia-Belmonte, F. Fabregat-Santiago, N.S. Ferriols, P. Bogdanoff, E.C. Pereira, Journal of Physical Chemistry B 104 (2000) 2287–2298.
[20] J. Bisquert, M. Gratzel, Q. Wang, F. Fabregat-Santiago, Journal of Physical Chemistry B 110 (2006) 11284–11290.
[21] P. Bjornbom, Electrochemistry Communications 9 (2007) 211–215.
[22] D. Dunn, J. Newman, Journal of the Electrochemical Society 147 (2000) 820–830.
[23] B. Pillay, J. Newman, Journal of the Electrochemical Society 143 (1996) 1806–1814.
[24] V. Srinivasan, J.W. Weidner, Journal of the Electrochemical Society 146 (1999) 1650–1658.
[25] M.W. Verbrugge, P. Liu, Journal of the Electrochemical Society 152 (2005) D79–D87.
[26] T. Fujita, L.H. Qian, K. Inoke, J. Erlebacher, M.W. Chen, Applied Physics Letters 92 (2008).
[27] P.N. Bartlett, J. Marwan, Chemistry of Materials 15 (2003) 2962–2968.
[28] S.W. Woo, K. Dokko, K. Kanamura, Journal of Power Sources 185 (2008) 1589–1593.
[29] L. Bazin, S. Mitra, P.L. Taberna, P. Poizot, M. Gressier, M.J. Menu, A. Barnabe, P. Simon, J.M. Tarascon, Journal of Power Sources (2009) 578–582.
[30] S.K. Cheah, E. Perre, M. Rooth, M. Fondell, A. Harsta, L. Nyholm, M. Boman, T. Gustafsson, J. Lu, P. Simon, K. Edstrom, Nano Letters 9 (2009) 3230–3233.
[31] A. Patil, V. Patil, D.W. Shin, J.W. Choi, D.S. Paik, S.J. Yoon, Materials Research Bulletin 43 (2008) 1913–1942.
[32] T.F. Baumann, M.A. Worsley, T.Y.J. Han, J.H. Satcher, Journal of Non-Crystalline Solids 354 (2008) 3513–3515.
[33] F. Chamran, Y. Yeh, H.S. Min, B. Dunn, C.J. Kim, Journal of Microelectromechanical Systems 16 (2007) 844–852.
[34] H.S. Min, B.Y. Park, L. Taherabadi, C.L. Wang, Y. Yeh, R. Zaouk, M.J. Madou, B. Dunn, Journal of Power Sources 178 (2008) 795–800.
[35] R.H. Nilson, S.K. Griffiths, Journal of Chemical Physics 125 (2006).
[36] J.R. Miller, Electrochimica Acta 52 (2006) 1703–1708.
[37] M.W. Verbrugge, P. Liu, Journal of the Electrochemical Society 153 (2006) A1237–A1245.
[38] M. Eikerling, A.A. Kornyshev, E. Lustd, Journal of the Electrochemical Society 152 (2005) E24–E33.
[39] R.H. Nilson, S.K. Griffiths, Physical Review E 79 (2009) 036304.
[40] R.H. Nilson, S.K. Griffiths, Physical Review E 80 (2009) 016310.
[41] J.W. Long, B. Dunn, D.R. Rolison, H.S. White, Chemical Reviews 104 (2004) 4463–4492.
[42] J.R. Miller, in: W.A. Adams, A.R. Landgrebe, B. Scrosati (Eds.), Exploratory Research and Development of Batteries for Electric and Hybrid Vehicles, vol. PV96-14, The Electrochemical Society, 1996, p. 16.
[43] P.V. Braun, P. Osenar, V. Tohver, S.B. Kennedy, S.I. Stupp, Journal of the American Chemical Society 121 (1999) 7302–7309.
[44] S. Parida, D. Kramer, C.A. Volkert, H. Rosner, J. Erlebacher, J. Weissmuller, Physical Review Letters 97 (2006).
[45] M.H. El-Husseini, P. Venet, G. Rojat, C. Joubert, IEEE Transactions on Industry Applications 38 (2002) 713–718.
[46] R.M. Wightman, D.O. Wipf, Electroanalytical Chemistry 15 (1989) 267–353.
[47] G.M. Schmid, R.N. Obrien, Journal of the Electrochemical Society 111 (1964) 832–837.
[48] Y. Oren, Desalination 228 (2008) 10–29.
[49] R.S. Deinhammer, E.Y. Ting, M.D. Porter, Analytical Chemistry 67 (1995) 237–246.
[50] J.S. Huang, B.G. Sumpter, V. Meunier, Chemistry: A European Journal 14 (2008) 6614–6626.
[51] J. Chmiola, G. Yushin, Y. Gogotsi, C. Portet, P. Simon, P.L. Taberna, Science 313 (2006) 1760–1763.
[52] H.J. Gores, J.M.G. Barthel, Pure and Applied Chemistry 67 (1995) 919–930.
[53] A. Nishino, Journal of Power Sources 60 (1996) 137–147.